2018 IGARSS (MOP2.PP.1-1025)

Geophysical turbulent characteristics inferred from observations of submesoscale surface currents and chlorophyll concentration maps

Sung Yong Kim[1,†] and Eun Ae Lee[1]

[1]Department of Mechanical Engineering Korea Advanced Institute of Science and Technology,
syongkim@kaist.ac.kr[†]

National Research Foundation of Korea

Abstract

The spectral characteristics of hourly and 1-km resolution coastal surface currents obtained from an array of high-frequency radars and surface passive tracers derived from geostationary ocean color imagery off the East Coast of Korea are described in the frequency and wavenumber domains. The primary variance of the observed surface currents for a period of one year appears in the low-frequency (longer than 2 days), diurnal, and near-inertial frequency bands. The low-frequency surface currents exhibit more consistent variability with the regional geostrophic currents in summer than those in winter because of the relatively weaker wind conditions and a shallower mixed layer during summer. The diurnal surface circulation contains components that are coherent with diurnal land-sea breezes because of the development of the diurnal marine boundary layer. Clockwise near-inertial surface currents show onshore phase propagations along with their decreasing amplitudes, represented as a coastal inhibition associated with coastal boundary effects on the near-inertial currents in coastal areas. The kinetic energy spectra of the surface currents in the wavenumber domain have decay slopes between k^{-2} and k^{-3}, and their seasonal decay slopes are slightly steeper in winter than in summer. The wavenumber domain kinetic energy (KE) spectra of the chlorophyll exhibit anisotropy associated with bathymetric effects and regional circulation, and their decay slopes change from $k^{-5/3}$ to k^{-1} at $O(10)$ km scales and from k^{-1} to k^{-3} at $O(1)$ km scales, which is consistent with the two-dimensional quasi-geostrophic turbulence theory. These findings can be interpreted that the submesoscale processes in this region can be related to both surface frontogenesis caused by regional mesoscale eddies with weak seasonality and baroclinic instability associated with the seasonal mixed layer and vertical fluctuations modulated by its harmonic frequencies.

Observations

Hourly averaged surface currents on a grid with a 1 km spatial resolution off the coast of Imwon, Republic of Korea for a period of one year (2013) have been obtained by two phased-array HFRs [WavE RAdar (WERA) system] of Imwon North (IMWN; R1) and Imwon South (IMWS; R2) (Figure 1b). Although the WERA-derived radial velocities are typically reported on a Cartesian coordinate grid for the convenience of vector current mapping, we internally modify scripts and obtain the radial velocities reported on the polar coordinate grids of individual HFRs, which allows us to investigate the characteristics of the radial velocity data prior to mapping and apply optimal interpolation (OI) to directly estimate the kinematic and dynamic quantities (e.g., stream function, velocity potential, divergence, vorticity, and strain rates) of surface currents with any intermediate steps. In this paper, OI uses an exponential correlation functions with an isotropic decorrelation length scales of 1.5 km to minimize spatial smoothing.

Hourly GOCI-derived products include the maps of CHLs, colored dissolved organic matter (CDOM), total suspended solids (TSS), concentration-derived vector currents, and eight-band images around the Korean Peninsula with a spatial resolution of 0.5 km. Due to passive mode observations, the meaningful GOCI L2A products are mainly obtained during daylight hours (e.g., maximum of eight snapshots a day). The raw GOCI data are subjected to multiple steps of filtering and calibration including an internal GOCI data processing system (GDPS). The L2A products are provided with the flag, i.e., pre-determined parameters for QAQC of the GOCI data. Probability density functions (PDFs) of the log-scaled CHL data are presented in terms of the flag (Figure 1c) and shows that the L2A CHL product with Flag3 is close to an approximately Gaussian distribution with a relative low density of outliers (Figure 1c), which can justify the techniques and analyses used in this paper (e.g., maximum likelihood estimate, covariance and correlation estimates, and least-squares).

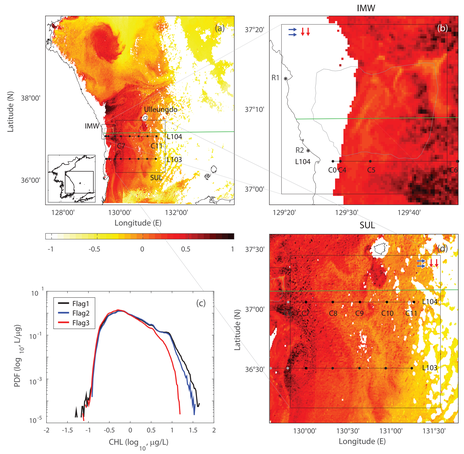

Figure 1: (a) An example of the GOCI-derived chlorophyll (CHL) concentration ($\log_{10}$, μg L^{-1}) off the East/Japan Sea (EJS), sampled on October 12, 2013. A coastal region (Imwon; IMW) and an open ocean area (South of Ulleungdo; SUL) are marked with black boxes. Stations (C0 to C11) on two hydrographic survey lines (L103 and L104) to sample temperature, density, and nutrients are denoted. (b) and (d): Close-up of two sub-domains [(b) IMW and (d) SUL].

Variance in the frequency domain

Significant variance in the surface currents appears in three frequency bands, specifically the non-zero low-frequency band [$0 < |\sigma| \leq 0.2$ cpd] for both rotations (clockwise and counter-clockwise), the clockwise diurnal frequency ($\sigma = -1$ cpd), and the clockwise near-inertial frequency band ($-1.4 \leq \sigma \leq -1.2$ cpd) (Figure 2a). These frequency bands are closely associated with the responses to the primary driving forces and regional currents of (1) the coastal circulation, which is related to the branches of the two regional boundary currents (NKCC and EKWC in Figure 1b) and the geostrophic currents; (2) diurnal land-sea breeze-driven surface responses; and (3) superinertially shifted clockwise motions, respectively.

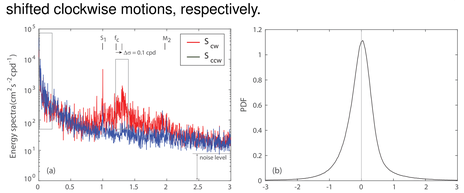

Figure 2: (a) Frequency-domain rotary spectra of the hourly surface vector currents are presented in the clockwise (S_{cw}) and counter-clockwise (S_{ccw}) rotations, averaged over 553 grid points (a gray curve in Figure 1c). Three primary frequency (and bands) are marked with lines and boxes including non-zero low-frequency band [$0 < |\sigma| \leq 0.2$ cpd] for both rotations (clockwise and counter-clockwise), clockwise diurnal frequency ($\sigma = -1$ cpd), and clockwise near-inertial frequency band ($-1.4 \leq \sigma \leq -1.2$ cpd; $f_c = 1.2078$ cpd at 37.15°N), A superinertially shifted peak appears in the clockwise rotation ($\Delta\sigma = 0.1$ cpd). The noise level is defined as the floor level at the Nyquist frequency (12 cpd). (b) A probability density function (PDF) of the normalized vorticity ($R_o = \zeta/|f_c|$).

Variance in the wavenumber domain

The wavenumber-domain energy spectra of surface currents have decay slopes between k^{-2} and k^{-3} (Figures 3a and 3c) with slight differences in the averaging direction, consistent with the energy spectra of coastal surface currents reported elsewhere. The seasonally averaged wavenumber-domain spectra have slightly steeper decay slopes in winter than in summer and higher variance in summer than in winter (Figures 3b and 3d), which an opposite pattern of the submesoscale processes associated with the seasonal mixed layer. The non-seasonal and persistent regional mesoscale currents and their branches near the coast may affect the generation of submesoscale frontogenesis.

To perform a more detailed investigation on the temporal variability of the spectral slopes, the spectral slopes of the wavenumber domain energy spectra [$S_x(k)$ and $S_y(k)$] are regressed within the individual wavenumber ranges [$0.04 \leq k_{1,x} \leq 0.1$ km^{-1} and $0.15 \leq k_2 \leq 0.4$ km^{-1} for $S_x(k)$; $0.06 \leq k_{1,y} \leq 0.14$ km^{-1} and $0.15 \leq k_2 \leq 0.4$ km^{-1} for $S_y(k)$] (see Figure 3c). Their mean and standard errors within a 10-day-long time window are then presented with the expected spectral slopes [k^{-1} (red), $k^{-5/3}$ (black), and k^{-3} (blue)] (Figures 3e and 3f).

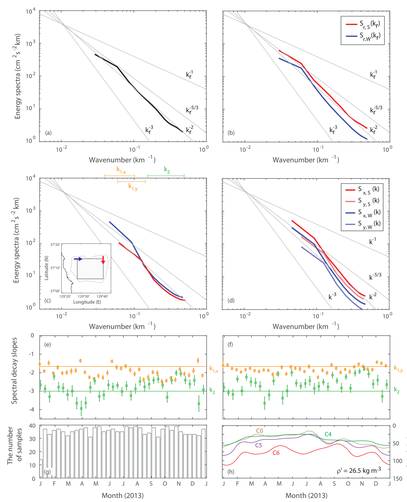

Figure 3: (a) and (b): Wavenumber domain energy spectra of the hourly radial velocities at IMWN in the range direction and seasons for a period of one year (2013) [$S_{r,S}(k)$ for summer (red) and $S_{r,W}(k)$ for winter (blue)]. The wavenumber domain energy spectra of the radial velocities sampled in the range direction are averaged in the azimuthal direction. (c) and (d): Wavenumber domain energy spectra of the hourly vector currents for a period of one year (2013) [$S_x(k)$ for cross-shore direction (blue) and $S_y(k)$ for along-shore direction (red)] and seasons [$S_{x,S}(k)$ (red) and $S_{y,S}(k)$ (light red) for summer; $S_{x,W}(k)$ (blue) and $S_{y,W}(k)$ (light blue) for winter]. (e) and (f): Spectral slopes are estimated from the energy spectra of six-hourly-averaged surface currents using a least-squares fit in individual wavenumber ranges. (g) The number of vector current maps participating in the estimates of the spectral slopes in Figures 3e and 3f (The bin size is equal to 10 days). (h) Time series of the depth of the constant density anomaly ($\rho' = 26.5$ kg m^{-3}).

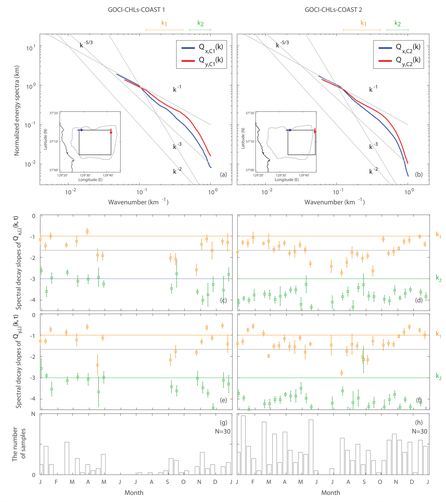

Figure 4: (a) and (b): Normalized wavenumber domain KE spectra of GOCI-derived CHLs (2011 to 2015) in two coastal regions – (a) an area completely overlapped with HFR-derive surface currents and (b) an area off 35 km from the coast. The KE spectra of the CHLs sampled on multiple one-dimensional cross-shore lines (x) are averaged in the along-shore direction (y) to estimate the wavenumber domain KE spectrum [$\mathcal{Q}_x(k)$] in the cross-shore direction. Similarly, $\mathcal{Q}_y(k)$ is the cross-shore-directional (x) average of the KE spectra estimated from surface currents sampled in the along-shore direction (y). (c) and (d): Spectral slopes of $\mathcal{Q}_x(k,t)$. (e) and (f): Spectral slopes of $\mathcal{Q}_y(k,t)$. (g) and (h): The number of CHL maps participating in estimating the spectral slope of the KE spectra in Figures 4c and 4f.

The estimated wavenumber domain KE spectra of the coastal CHLs [$\mathcal{Q}_{c1}(k)$ and $\mathcal{Q}_{c2}(k)$; IMW] in both directions have decay slopes of k^{-1} ($\lambda > \lambda_D$; $\lambda_D = 3$ km) and k^{-3} ($\lambda \leq \lambda_D$) (Figures 4a and 4b), which are nearly consistent with the spectral slopes of the KE spectra of the HFR-derived surface currents (k^{-2} and k^{-3} at the scale of 2 km) sampled in the same region. This can be explained by the QG theory and turbulent flows under geostrophic bathymetric effects with spectral slopes of k^{-3} and $k^{-2.5}$ at a scale of $O(1)$ km, respectively. Although the zonal and meridional CHL KE spectra have minor changes in their variance and spectral slopes and there are limited observations available in summer (June and July), the spectral slopes for the forward cascades ($\lambda > \lambda_D$) show seasonality along with semi-seasonal fluctuations of k^{-2} for summer and k^{-1} for winter, which can be explained with the baroclinic instability associated with the (seasonal) mixed layer (Figures 4c, 4d, 4e, and 4f). In addition, the spectral slopes below the dissipation scale ($\lambda \leq \lambda_D$) appear to be nearly out of phase compared with those above the dissipation scale or weak seasonality.

The estimated wavenumber domain KE spectra of the open ocean CHLs [$\mathcal{Q}_o(k)$; SUL] in both directions have decay slopes of $k^{-5/3}$ ($\lambda > \lambda_I$, $\lambda_I = 10$ km), k^{-1} ($\lambda_D < \lambda \leq \lambda_I$), and k^{-3} ($\lambda \leq \lambda_D$) (Figure 5a and 5b). These spectral slopes can be interpreted that the forward cascades of enstrophy (square of gradient of buoyancy) and inverse cascades of energy appear at the injection scale [$\lambda_I = O(10)$ km], where the baroclinic instability in the mixed layer plays a dominant role as the submesoscale driver rather than the mesoscale eddy-derived surface frontogenesis at a scale of $O(100)$ km [e.g., [1, 2]], and the surface dissipation scales are found near $O(1)$ km. The KE spectra of the HFR-derived surface currents do not clearly show the dissipation scale due to limited spatial scale of observations ($\lambda \geq 2$ km) [[3]]. The spectral slopes in the forward cascades ($\lambda > \lambda_I$; k_1 and k_1^*) and inverse cascades ($\lambda_I \leq \lambda < \lambda_D$; k_2) show seasonality (Figures 5c to 5f). In addition, the spectral slopes in dissipation ($\lambda \leq \lambda_D$; k_3) are slightly out of phase with those in two wavenumber ranges (k_1, k_1^*, and k_2) (Figures 5c and 5e). The number of data used in the KE spectrum estimates is not uniformly distributed, which may have temporal bias in January, February, June, July, November, and December (Figures 5g to 5i). Excluding the estimated spectral slopes in these time periods, the spectral slopes have seasonality along with semi-seasonal fluctuations becoming steeper in summer and flatter in winter (Figures 5c to 5f).

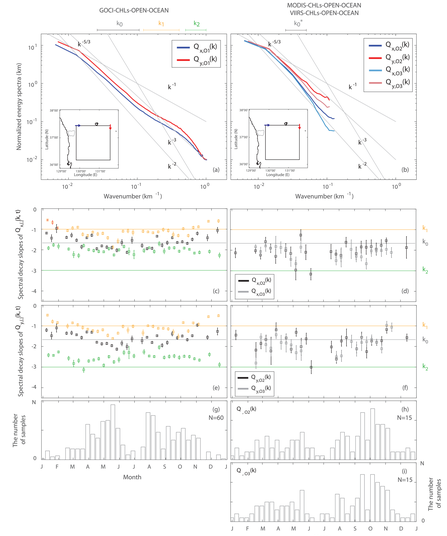

Figure 5: (a) and (b): Normalized wavenumber domain KE spectra of CHLs in the open ocean area [$\mathcal{Q}_o(k)$, SUL]. (a) GOCI-derived CHLs [2011 to 2015; $\mathcal{Q}_{o1}(k)$]. (b) MODIS-derived CHLs [2011 to 2015; $\mathcal{Q}_{o2}(k)$] and VIIRS-derived CHLs [2012 to 2015; $\mathcal{Q}_{o3}(k)$]. (c) and (d): Spectral slopes of $\mathcal{Q}_x(k,t)$. (e) and (f): Spectral slopes of $\mathcal{Q}_y(k,t)$. (g) to (i): The number of CHL maps participating in estimating the spectral slope of the KE spectra.

Acknowledgement

This work is supported by a grant through the National Research Foundation (NRF), Ministry of Education (NRF-2017R1D1A1B03028285), Republic of Korea.

References

[1] R. Ferrari and C. Wunsch. Ocean circulation kinetic energy: Reservoirs, sources, and sinks. *Annu. Rev. Fluid Mech.*, 41:253–282, 2009.

[2] Ross Tulloch, John Marshall, Chris Hill, and K Shafer Smith. Scales, growth rates, and spectral fluxes of baroclinic instability in the ocean. *J. Phys. Oceanogr.*, 41(6):1057–1076, 2011.

[3] J. G. Yoo, S. Y. Kim, and H. S. Kim. Spectral descriptions of submesoscale surface circulation in a coastal region. *J. Geophys. Res.*, 123, 2018. in press.